

Phonon-pump electronic-probe study of methylammonium lead iodide reveals electronically decoupled organic and inorganic sublattices

Peijun Guo¹, Arun Mannodi-Kanakkithodi¹, Jue Gong², Yi Xia¹, Constantinos C. Stoumpos³, Duyen H. Cao⁴, Benjamin T. Diroll¹, John B. Ketterson⁵, Gary P. Wiederrecht¹, Tao Xu², Maria K. Y. Chan¹, Mercouri G. Kanatzidis³, Richard D. Schaller^{1,3,*}

¹*Center for Nanoscale Materials, Argonne National Laboratory, 9700 South Cass Avenue, Lemont, IL 60439, United States*

²*Department of Chemistry and Biochemistry, Northern Illinois University, 1425 W. Lincoln Hwy., DeKalb, IL 60115, United States*

³*Department of Chemistry, Northwestern University, 2145 Sheridan Road, Evanston, IL 60208, United States*

⁴*Materials Science Division, Argonne National Laboratory, 9700 South Cass Avenue, Lemont, IL 60439, United States*

⁵*Department of Physics and Astronomy, Northwestern University, 2145 Sheridan Road, Evanston, IL 60208, United States*

Abstract

Organic-inorganic hybrid perovskites such as methylammonium lead iodide ($\text{CH}_3\text{NH}_3\text{PbI}_3$) are game-changing semiconductors for solar cells¹ and light-emitting devices² owing to their exceptionally long carrier lifetime and diffusion length³. Determining whether the large dipole moment of the organic cation and dynamic disorder benefit the optoelectronic properties of $\text{CH}_3\text{NH}_3\text{PbI}_3$ has been an outstanding challenge^{4,5}. Herein, via transient absorption measurements employing an infrared pump pulse tuned to a methylammonium vibration, we observe slow, nanosecond-long thermal dissipation from the selectively excited organic mode to the entire lattice. Resulting transient electronic signatures, during the period of thermal-nonequilibrium when the induced thermal motions are mostly concentrated on the organic sublattice, reveal that induced motions of the organic cations do not alter absorption or photoluminescence response of $\text{CH}_3\text{NH}_3\text{PbI}_3$, beyond thermal effects. Our results suggest that the attractive optoelectronic properties of $\text{CH}_3\text{NH}_3\text{PbI}_3$ mainly derive from the inorganic lead-halide framework⁶⁻⁸.

Hybrid perovskites, including the prototypical $\text{CH}_3\text{NH}_3\text{PbI}_3$, present challenges in understanding the interplay between structural and optoelectronic properties. This primarily stems from significant dynamic disorder of the organic cations (CH_3NH_3^+) with picosecond, observed relaxation times^{4,9}. Due to crucial importance for enhancing device efficiency¹⁰ and enabling new functionalities^{11,12}, the mutual interactions between the fluctuating dipolar organic cations and charge carriers that reside on the inorganic Pb-I framework have been extensively investigated. Formation of (anti)ferroelectric domains arising from polar organic cations was proposed to enhance carrier lifetimes¹³, but spectroscopic measurement did not support such a picture¹⁴. Dynamic bulk Rashba effect induced by the CH_3NH_3^+ cations was also suggested^{15,16}, yet recent theoretical and experimental results show that such an effect is negligible¹⁷. In fact, $\text{HC}(\text{NH}_2)_2\text{PbI}_3$ -based devices exhibit conversion efficiencies comparable to the $\text{CH}_3\text{NH}_3\text{PbI}_3$ analog¹⁸, albeit the dipole moment of $\text{HC}(\text{NH}_2)_2^+$ is much smaller than that of CH_3NH_3^+ (ref¹³). Although comparative studies between hybrid and all-inorganic perovskites have been attempted so as to evaluate the role of polar organic cations on material performance¹⁹⁻²¹, the properties of metal-halide perovskites are known to depend on synthetic conditions and material history^{22,23}. Experimental approaches permitting direct investigation of interactions between the organic and inorganic sublattices in hybrid systems are thereby important.

Here, we employ infrared-pump electronic-probe (IPEP) spectroscopy, to excite strongly-absorbing vibrational modes of the organic sublattice and examine the corresponding optical response near the bandgap of $\text{CH}_3\text{NH}_3\text{PbI}_3$. Fig. 1a maps the temperature dependent static absorption of a $\text{CH}_3\text{NH}_3\text{PbI}_3$ thin film around its bandgap. The tetragonal-to-orthorhombic phase transition near 145 K is denoted by an abrupt change of bandgap, and for each individual phase the bandgap increases with temperature. The near-bandgap, distinct absorption peak in the orthorhombic phase arises due to a comparatively stronger excitonic character. Fig. 1b presents temperature-dependent static absorption arising from N-H asymmetric stretching modes (abbreviated here as N-H-*as* modes) of the CH_3NH_3^+ cation, which exhibit the strongest absorption cross-section among various vibrational modes of the molecular cation²⁴. A dramatic increase of the N-H-*as* absorption accompanying the phase transition is due to the formation of hydrogen bonding that suppresses rotational motions of CH_3NH_3^+ in the orthorhombic phase²⁵. The pronounced mid-infrared absorption, in conjunction with the near-bandgap absorption

feature, facilitate infrared-pump electronic-probe experiments on the orthorhombic phase of $\text{CH}_3\text{NH}_3\text{PbI}_3$.

In transient absorption measurements, we selectively pumped the N-H-*as* modes (centered at 3120 cm^{-1} ; Fig. S1) and probed the change of optical density (ΔOD) near the bandgap. The ΔOD spectral map acquired on $\text{CH}_3\text{NH}_3\text{PbI}_3$ at 10 K is displayed in Fig. 1c. We observe a derivative-like transient spectral response, where magnitude following excitation starts from zero, grows with pump-probe time delay, and saturates on the nanosecond timescale. Positive ΔOD signal on the blue side of the static absorption peak and negative signal to the red conveys a spectral blueshift, consistent with transient lattice heating (Fig. 1a). Note that large bandgap shifts arising from the optical Stark effect were observed at zero delay time, when the pump and probe pulses temporally overlapped²⁶ (Fig. S2). An off-resonance pump (centered at 2200 cm^{-1}) results in negligible transient response (Fig. S3), confirming that the response shown in Fig. 1c is due to vibrational excitation of the organic sublattice. The nanosecond timescale relates slow down-conversion of thermal energy from the high-energy N-H-*as* modes to the low-lying, cold phonon bath, with the latter encompassing all CH_3NH_3^+ modes except the N-H-*as* modes, and all the modes of the inorganic sublattice.

Probing the tetragonal crystal phase at 205 K distills a comparably faster thermal equilibration with a timescale of hundreds of picoseconds (Fig. S4). Measurement near the phase transition ($\sim 145\text{ K}$) reveals that the two coexisting phases respond independently to the pump (Fig. 1d), as no evidence of transient phase change is observed, which would otherwise lead to the transfer of spectral weight between the two phases. The ΔOD amplitude near the bandgap obtained for the tetragonal phase is, as expected, weaker than that for the orthorhombic counterpart, owing to a weaker vibrational absorption (Fig. 1b). The nearly identical timescales of ΔOD kinetics for the co-existing phases at 140 K (Fig. S4d) indicate that the rotations of CH_3NH_3^+ , which are only present in the tetragonal phase, do not apparently influence phonon-phonon coupling strength between the two sublattices. Temperature-dependent kinetics (Fig. 2a) present slower thermal equilibration at lower temperatures. Furthermore, the ΔOD amplitude increases with decreasing temperature (Fig. 2b), which results from the heat capacity that diminishes, and the absorption cross-section of N-H-*as* modes that grows, with decreasing temperature. Fluence-dependent measurements (Fig. 2c) show that the ΔOD amplitude scales

nearly linearly with pump fluence, and the thermal equilibration time is not sensitive to pump fluence over the explored range, consistent with earlier work based on transient mid-infrared spectroscopy using electronic excitation and an infrared probe²⁴.

Having established the transient response with IPEP, we then turn to investigating whether perturbatively induced motions of the organic sublattice influence the near-bandgap optical properties of $\text{CH}_3\text{NH}_3\text{PbI}_3$. As illustrated in Fig. 3a, following the selective excitation of N-H-*as* modes, phonon-phonon scattering leads to the sequential population of various lower-energy CH_3NH_3^+ vibrational modes, and ultimately the population of inorganic phonon modes. Note that thermal equilibration within the inorganic sublattice itself requires only 10~20 ps, as reported elsewhere⁶. Therefore, the nanosecond timescale is mainly attributed to (1) slow intramolecular vibrational relaxation (IVR) within the CH_3NH_3^+ cations²⁷, supported by the relatively small phonon scattering phase space located in the 200~3000 cm^{-1} range (Fig. 3a); (2) slow energy transfer from CH_3NH_3^+ to the inorganic framework²⁴. To gain more insights into the vibrational evolution, we performed ab-initio molecular dynamics simulations on structures with selective excitation of the N-H-*as* modes based on the phonon calculations (see Supplementary Note 1), from which we extracted atomic trajectories up to ~130 ps. As shown in Fig. 3b, selective excitation of N-H-*as* modes results in the population of stretching modes as represented by the variation of bond lengths of N-H, C-H and C-N. The C-N bond-length variation decays more slowly in comparison to the C-H and N-H bonds, as the latter two are associated with vibrational modes of highest frequencies and depopulate most rapidly via IVR. Note that librational motions, captured by the orientational variation of the C-N bond (Fig. 3c), can also be induced. The simulated timescale is furthermore not strongly dependent on the total imparted energy in the simulations, which is consistent with the experimental results (Fig. 2c).

The change in amplitude of transient optical signal can act as a proxy for how much thermal energy has been transferred to the inorganic framework (that in turn determines the bandgap). The transient response at long delay time (>1000 ps), when the sample has reached thermal equilibrium (Fig. 2a), results from the change of bandgap with temperature. Transient spectra plotted for representative delay times (Fig. 3d) during the thermal relaxation closely overlap with a simple scaling of amplitude. Such spectral similarity suggests that no net increase or decrease of optical absorption coefficient, other than that caused by lattice heating, occurs upon this

perturbation when $\text{CH}_3\text{NH}_3\text{PbI}_3$ is at *thermal non-equilibrium* (i.e., 0~1000 ps). Because optical absorption can be viewed as an inverse process of bimolecular recombination²⁸, Fig. 3d implicitly suggests that pump-induced CH_3NH_3^+ motions do not impact bimolecular recombination in $\text{CH}_3\text{NH}_3\text{PbI}_3$.

IPEP measurements on $\text{CH}_3\text{NH}_3\text{PbBr}_3$ reveal similar transient optical response (Fig. S5) compared to $\text{CH}_3\text{NH}_3\text{PbI}_3$ due to their structural similarity. However, in contrast to $\text{CH}_3\text{NH}_3\text{PbI}_3$ and $\text{CH}_3\text{NH}_3\text{PbBr}_3$ which are three-dimensional perovskites, impact of artificially induced organic cation motion is observed for the two-dimensional perovskite, $(\text{CH}_3(\text{CH}_2)_3\text{NH}_3)_2\text{PbI}_4$. For this compound²⁹, the $\text{CH}_3(\text{CH}_2)_3\text{NH}_3^+$ cations situated between the perovskite layers strongly impact the electronic properties through both quantum and dielectric confinement effects. Following selective vibrational excitation near 3100 cm^{-1} (Fig. S6), a much faster transient response, relative to the 3D counterparts, was observed for $(\text{CH}_3(\text{CH}_2)_3\text{NH}_3)_2\text{PbI}_4$ near the exciton energy (Fig. S5), owing to IVR processes of the $\text{CH}_3(\text{CH}_2)_3\text{NH}_3^+$ cations that in turn alters the strength of quantum confinement of the electron-hole pairs (i.e., excitons) residing on the Pb-I framework.

We further explored if the infrared-pump-induced CH_3NH_3^+ motions can directly impact photoluminescence (PL) of $\text{CH}_3\text{NH}_3\text{PbI}_3$, using infrared-pump PL-probe measurements based on the schematic shown in Fig. S7. Here, the pump pulse was followed by a time delayed (denoted as Δt), low-intensity, 400-nm PL-probe pulse that generates electron-hole pairs (positive Δt is defined if the infrared pump hits the sample first). The emitted photons were either detected by a CCD camera, or spectrally and temporally resolved by a streak camera. Fig. 4a presents a representative, spectrally-resolved PL map measured at 50 K without using the infrared pump. Fig. 4b shows the spectrally-integrated PL decay kinetics measured under various negative values of Δt , with the infrared pump turned on. The dip in the PL decay trace, which exhibits an instrument-response-time-limited timescale, is also observed by using an off-resonant mid-infrared pump (Fig. S8), and therefore attributed to electric-field driven dissociation of electron-hole pairs, or the optical Stark effect. We then focused on measurements under positive Δt values. Fig. 4c presents PL decays measured using different positive Δt values that traverse the duration of sublattice thermal-equilibration. We find that optically pumping the organic vibrational modes of $\text{CH}_3\text{NH}_3\text{PbI}_3$ does not alter the carrier recombination rate.

While streak camera measurements only detect PL over specific time windows, time-integrated PL measurements with higher signal-to-noise ratio can reveal whether the infrared-pump-induced CH_3NH_3^+ motions can enhance (by suppressing defect scattering of charge carriers) or suppress (by slowing down the recombination rate of carriers so that more trapping events can take place) the brightness of $\text{CH}_3\text{NH}_3\text{PbI}_3$. Static, temperature dependent PL intensity (Fig. 4d) suggests that a substantial portion of photo-generated carriers are still lost through non-radiative decay pathways at 50 K. The time-integrated PL spectra measured at 10 K and 50 K are shown in Fig. 4e; note that the dramatic change in PL linewidth upon temperature reduction has been observed previously³⁰. For both temperatures, the infrared pump ($\Delta t=2000$ ps) yields a blueshift of the PL spectrum, stemming from a bandgap increase due to lattice heating. We ran measurements at these two temperatures because the fast PL decay component due to bimolecular recombination³¹ is commensurate with the thermal equilibration time, and hence the impact of non-equilibrium CH_3NH_3^+ motions, if there are any, can be more pronounced. Based on the PL spectral shift at 50 K (in conjunction with data in Fig. 1a and heat capacity³²), we estimate that 0.06 photons are absorbed per orthorhombic unit cell by CH_3NH_3^+ , with a photon energy of 386 meV (corresponding to 3120 cm^{-1}). We denote the change of PL counts at each wavelength as $\Delta N=N_{\text{on}}-N_{\text{off}}$, where N_{on} (N_{off}) designates PL counts obtained with (without) the infrared pump. The spectra of $\Delta N/I_{\text{tot}}$ measured at 10 K and 50 K using variable positive Δt values are presented in Fig. 4f and 4g, respectively, where I_{tot} is the spectrally-integrated total PL counts measured without the infrared pump. At 10 K, infrared pumping yields a PL blueshift, the magnitude of which increases with Δt . This arises since with a larger Δt , more photons were emitted subsequent to more substantial sample heating, which produces a stronger bandgap increase. A similar PL blueshift is observed also at 50 K, although an additional increase of PL intensity, implied by an asymmetric line-shape, is observed especially for small Δt values. To explore the origin of such PL enhancement, we ran control experiments with an off-resonance infrared pump centered at 2200 cm^{-1} . As shown in Fig. 4h, although the PL blueshift is no longer present due to the lack of lattice heating, a PL intensity enhancement is still recovered. The observed PL enhancement retained using both pumping wavelengths is likely attributable to polaron formation arising from below-bandgap excitation of various phonon modes of the inorganic sublattice (evident from Fig. S9)⁸, that may contribute to protection of charge carriers from defect scattering. This effect is not clearly observable at 10 K since the $\Delta N/I_{\text{tot}}$ intensity

arising from bandgap blueshift is an order of magnitude larger than in the 50-K measurement. Importantly, comparison of Fig. 4g and 4h reveals that the induced CH_3NH_3^+ motions alone leads to negligible variation of the integrated PL intensity.

Our transient absorption and PL measurements both suggest that infrared-pump induced CH_3NH_3^+ motions do not lead to noticeable changes of the near-bandgap absorption and PL properties, beyond effects due to lattice heating. Such an observation implies that photo-generated carriers residing on the inorganic sublattice are essentially decoupled from the dynamically disordered organic cations. This conclusion is consistent with the long carrier lifetimes (exceeding 10 μs) of high-quality, fully-inorganic perovskite CsPbI_3 , and remarkable solar cell efficiencies derived from such^{33,34}. The novel spectroscopic technique reported here, complementary to fully electronic pump-probe measurements^{35,36}, can be generalized for studying organic semiconductors, organic-inorganic interfaces, and other organic-inorganic hybrid materials such as superatomic solids³⁷ and two-dimensional hybrid perovskites²⁹.

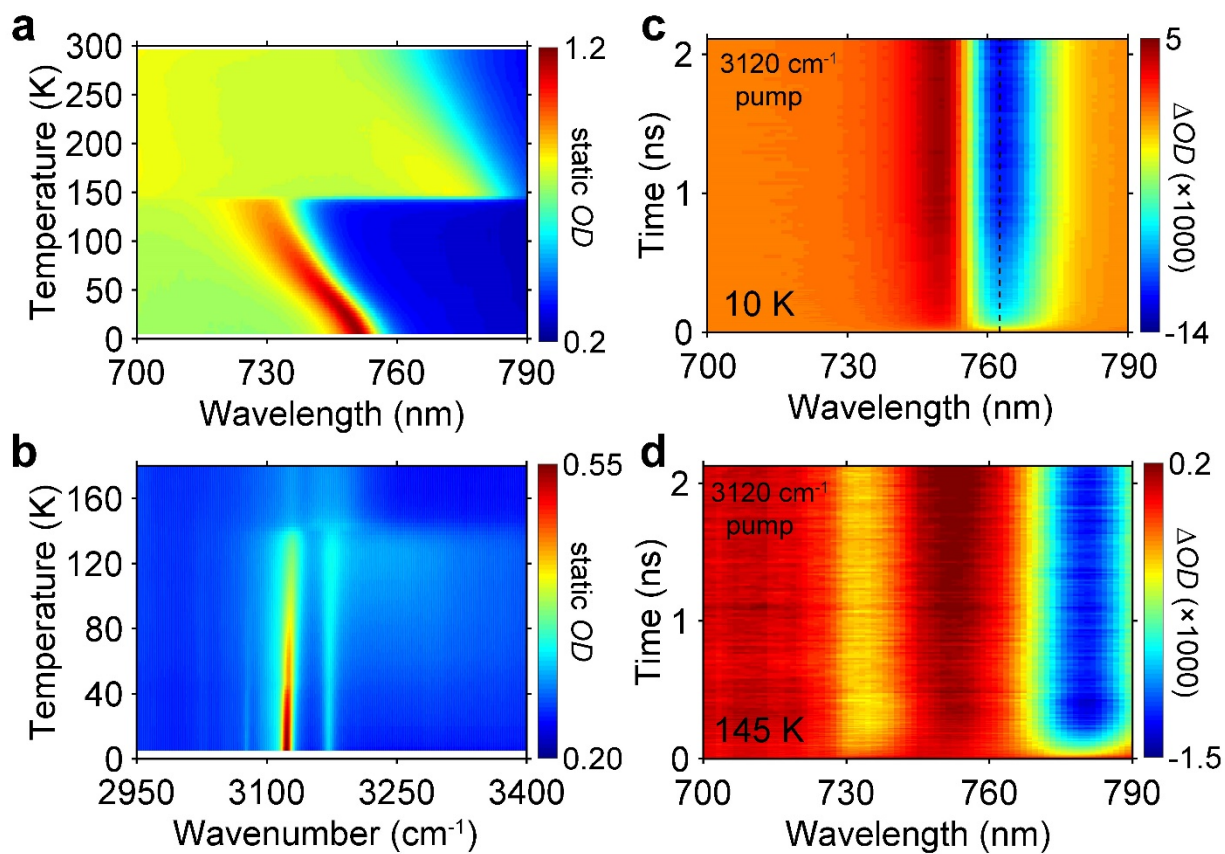


Figure 1. Static and IPEP measurements of $\text{CH}_3\text{NH}_3\text{PbI}_3$. **a** Static, temperature-dependent absorption around the bandgap. **b** Static, temperature-dependent absorption around the N-H-*as* vibrational modes. **c** ΔOD spectral map measured with on-resonance infrared pump (centered at 3120 cm^{-1}) at 10 K. The dashed line shows the wavelength at which the kinetics are extracted (Fig. 2a). **d** ΔOD spectral map measured at 145 K with on-resonance infrared pump. Fluence in **c** and **d** was $0.45\text{ mJ}\cdot\text{cm}^{-2}$.

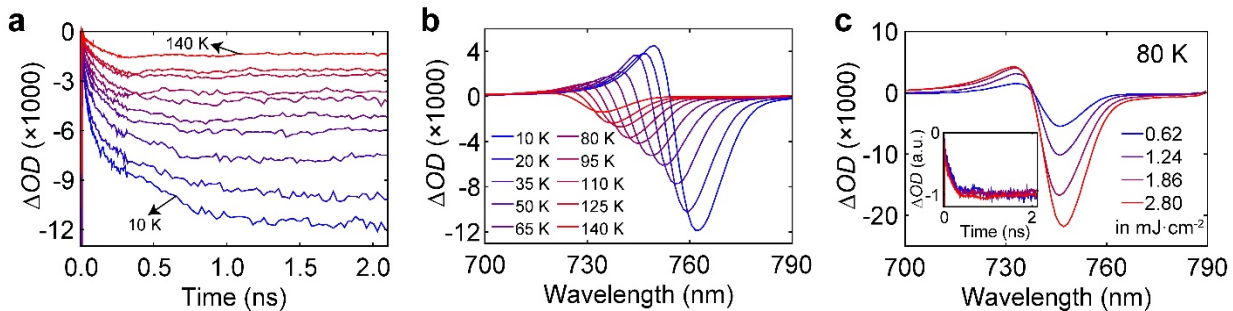


Figure 2. Temperature and fluence dependent transient optical response. **a** Transient kinetics at the wavelength indicated by the dashed line in Fig. 1c, measured at different temperatures. **b** Transient spectra at 2-ns delay time measured at different temperatures. Legend in **b** applies to **a** as well. Pump fluence used in **a** and **b** was $0.45 \text{ mJ}\cdot\text{cm}^{-2}$. **c** Fluence-dependent transient optical spectra at 2-ns delay time; inset: kinetics for different fluences appear nearly unchanged.

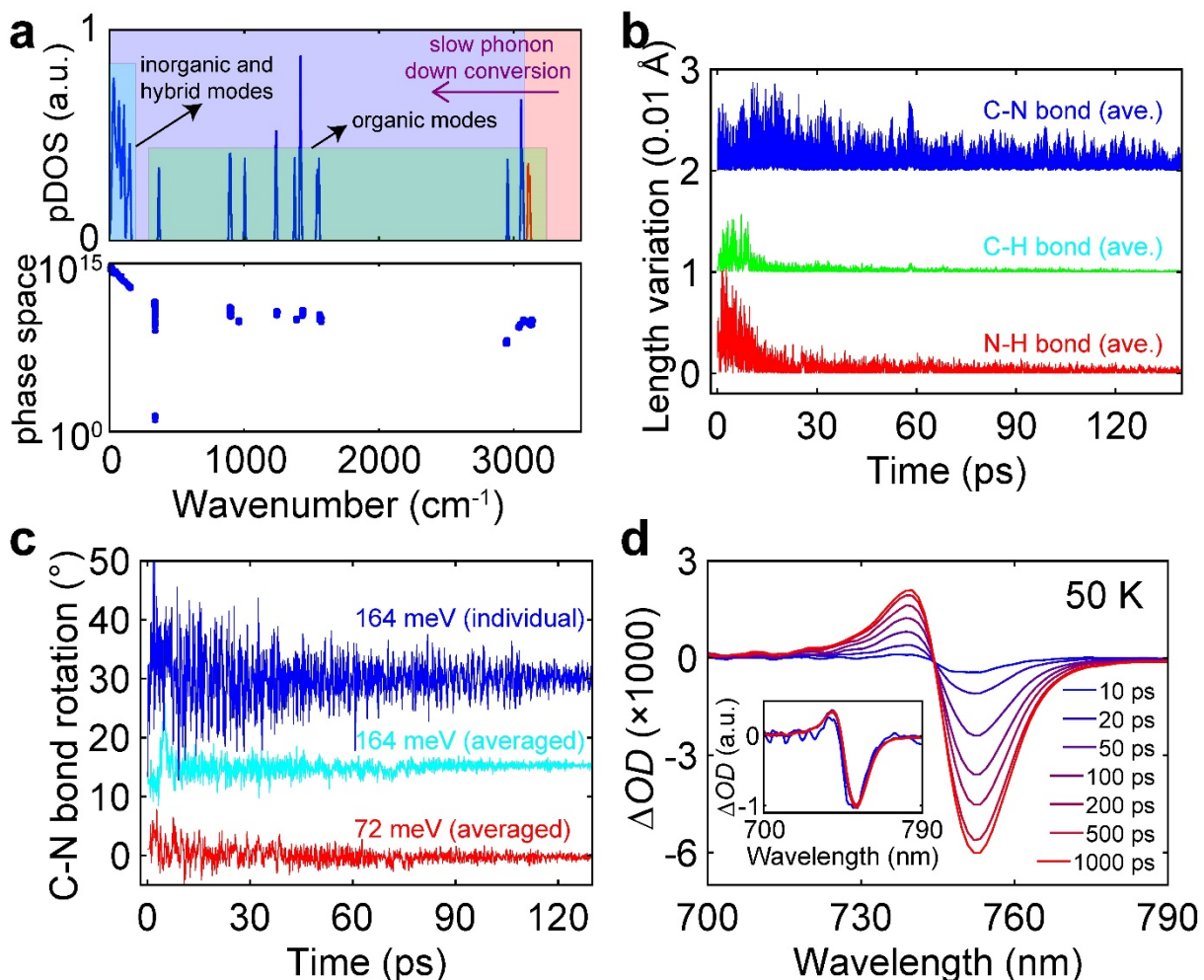


Figure 3. First-principles calculation of phonon dynamics for orthorhombic $\text{CH}_3\text{NH}_3\text{PbI}_3$. **a** Calculated zero-Kelvin phonon density of states (pDOS) and phonon scattering phase space. **b** Absolute variation in the N-H, C-H and C-N bond lengths from AIMD simulations. Data are averaged over the four CH_3NH_3^+ cations in the orthorhombic unit cell. Initial imparted energy is 164 meV. **c** Variation in the C-N bond angle for different amounts of energies imparted into the unit cell. Blue curve is for a representative C-N bond; cyan and red curves are data averaged over all the four CH_3NH_3^+ cations in the orthorhombic unit cell. Data in **b** and **c** are offset for clarity. **d** Transient spectra acquired at several different delay times; inset shows the overlapped transient spectra in arbitrary units by simple scaling. Fluence used was $0.45 \text{ mJ}\cdot\text{cm}^{-2}$.

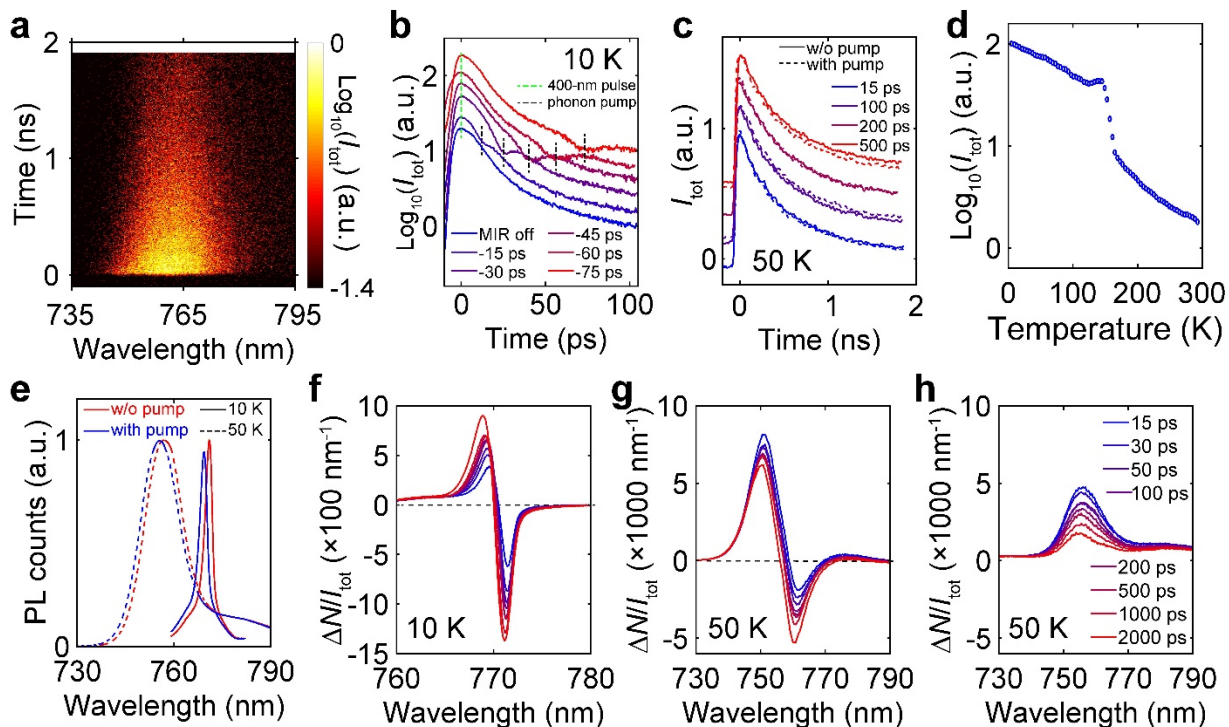


Figure 4. Infrared-pump PL-probe measurements of $\text{CH}_3\text{NH}_3\text{PbI}_3$. **a** Spectrally and temporally resolved PL counts measured with a streak camera; infrared pump was turned off. **b** PL intensity decay kinetics acquired under various negative Δt values. **c** Comparison of PL intensity decay kinetics acquired under various positive Δt values, with (dashed lines) and without (solid lines) using the infrared pump. **d** Static, temperature-dependent, integrated PL intensity of the measured $\text{CH}_3\text{NH}_3\text{PbI}_3$ film. **e** Time-integrated PL spectra acquired at 10 K and at 50 K, with $\Delta t=2000$ ps. Relative change of the time-integrated PL spectra with various positive delay times measured at 10 K in **f**, and measured at 50 K in **g** and **h**. On-resonance infrared pump was used in **e**, **f**, **g**; off-resonance (2200 cm^{-1}) infrared pump was used in **h**. Fluence of the infrared pump was fixed at $3.8\text{ mJ}\cdot\text{cm}^{-2}$ in all the measurements. Legend in **h** also applies to **f** and **g**.

Methods

Chemicals and CH₃NH₃I synthesis. Methylamine solution (CH₃NH₂, 40 wt. % in H₂O), N-methyl-2-pyrrolidinone (NMP) and γ -Butyrolactone (GBL, $\geq 99\%$) were purchased from Aldrich. Hydriodic acid (HI, 57 wt. % in H₂O) and lead(II) iodide (PbI₂, 99.9985% metals basis) were purchased from Alfa Aesar. Ethyl ether (anhydrous) and acetone were obtained from Fisher Chemical. All chemicals were used as received without further purification. Equimolar of HI was dropwise added to CH₃NH₂ with stirring in a 50-mL round bottom flask immersed in ice bath, followed by rotary evaporation at 60 °C to dry off the solvent. Next, white solid was obtained and washed with excessive ethyl ether on filter paper, as accompanied with vacuum filtration. Washed CH₃NH₃I powder was then dried in a vacuum oven at 60 °C overnight to yield final product.

CH₃NH₃PbI₃ thin film fabrication. The preparation of CH₃NH₃PbI₃ thin film follows method reported previously with slight modification³⁸. 1.2:1 molar ratio of CH₃NH₃I/PbI₂ was dissolved in 1:1 volume ratio of NMP/GBL to make a 40 wt. % precursor solution. Then, precursor solution was spun-coated on an acetone-cleaned sapphire substrate with a speed of 3000 rpm for 30 s. Next, as-formed wet film was quickly transferred into an ethyl ether bath (50 mL) for 90 s. Finally, developed film was dried in air, covered by a petri dish, and followed by annealing at 150 °C for 15 mins on a hot plate in a humidity-controlled environment.

Static optical characterization

Static infrared absorbance spectra were captured by FTIR (Thermo Nicolet 6700). Static visible absorbance spectra were obtained with a customized setup. In all the optical measurements (both static and transient), the samples were mounted in a 4-K closed-cycle cold-finger cryostat under with a base pressure below 1×10^{-7} Torr.

Transient absorption measurement

Transient absorption measurements were performed using a 35-fs amplified titanium:sapphire laser operating at 800 nm at a repetition rate of 2 kHz. Broadband visible probe pulses were generated by focusing a portion of the amplifier output into an Al₂O₃ window. Infrared pump pulses were generated by difference frequency mixing of signal and idler beams using an optical parametric amplifier and were reduced in repetition rate to 1 kHz. The probe pulses were

mechanically time delayed using a translation stage and retroreflector. Full transient spectral maps are shown in Fig. S10 and S11.

Infrared-pump PL-probe measurement

Generation of the infrared pump pulse was identical to that employed in the transient absorption measurements. 400-nm PL excitation pulses were produced by frequency-doubling of the 800-nm amplifier output with a BBO crystal and underwent similar beam path as the visible probe pulses in the transient absorption measurements. Both the infrared pump pulses and the 400-nm PL excitation pulses were maintained at 2 kHz. Temporally and spectrally resolved PL data were collected with a streak camera. Time-integrated PL data were captured with a CCD camera. The spot size of the 400-nm PL excitation pulses was adjusted to be smaller than that of the infrared pump pulses. The fluence of 400-nm PL excitation pulse was kept below $1 \mu\text{J}\cdot\text{cm}^{-2}$.

Additional Information

Supplementary information is available in the online version of the paper. Correspondence and requests for materials should be addressed to R.D.S. (schaller@anl.gov, schaller@northwestern.edu).

Author contributions

P.G. conceived the infrared-pump electronic-probe measurements under the supervision of R.D.S.. J.G., C.C.S., D.H.C. and B.T.D. fabricated the samples under the supervision of T.X., M.K.G. and R.D.S.. A.M.-K. and Y.X. performed first-principles calculations under the supervision of M.K.Y.C.. G.P.W. and J.B.K. contributed to the experiments and analysis. P.G. wrote the manuscript with input from all authors. R.D.S. supervised the project.

Notes

The authors declare no competing financial interests.

Acknowledgements

The work was performed at the Center for Nanoscale Materials, a U.S. Department of Energy Office of Science User Facility, and supported by the U.S. Department of Energy, Office of Science, under Contract No. DE-AC02-06CH11357. This material is based upon work supported by Laboratory Directed Research and Development (LDRD) funding from Argonne National

Laboratory, provided by the Director, Office of Science, of the U.S. Department of Energy under contract DE-AC02-06CH11357. Work at Northwestern University was supported by grant SC0012541 from the US Department of Energy, Office of Science (sample preparation). T.X. acknowledges the financial support from National Science Foundation (DMR-1806152). We thank Dr. A. B. F. Martinson for comments on the paper.

References

1. Lee, M.M., Teuscher, J., Miyasaka, T., Murakami, T.N. & Snaith, H.J. Efficient Hybrid Solar Cells Based on Meso-Superstructured Organometal Halide Perovskites. *Science* (2012).
2. Jia, Y., Kerner, R.A., Grede, A.J., Rand, B.P. & Giebink, N.C. Continuous-wave lasing in an organic–inorganic lead halide perovskite semiconductor. *Nat. Photonics* **11**, 784-788 (2017).
3. Xing, G. et al. Long-Range Balanced Electron- and Hole-Transport Lengths in Organic-Inorganic $\text{CH}_3\text{NH}_3\text{PbI}_3$. *Science* **342**, 344-347 (2013).
4. Leguy, A.M.A. et al. The dynamics of methylammonium ions in hybrid organic–inorganic perovskite solar cells. *Nat. Commun.* **6**, 7124 (2015).
5. A., E.D. et al. What Remains Unexplained about the Properties of Halide Perovskites? *Adv. Mater.* **30**, 1800691 (2018).
6. Wu, X. et al. Light-induced picosecond rotational disordering of the inorganic sublattice in hybrid perovskites. *Sci. Adv.* **3** (2017).
7. Yaffe, O. et al. Local Polar Fluctuations in Lead Halide Perovskite Crystals. *Phys. Rev. Lett.* **118**, 136001 (2017).
8. Miyata, K. et al. Large polarons in lead halide perovskites. *Sci. Adv.* **3** (2017).
9. Poglitsch, A. & Weber, D. Dynamic disorder in methylammoniumtrihalogenoplumbates (II) observed by millimeter-wave spectroscopy. *J. Chem. Phys.* **87**, 6373-6378 (1987).
10. Wang, L., McCleese, C., Kovalsky, A., Zhao, Y. & Burda, C. Femtosecond Time-Resolved Transient Absorption Spectroscopy of $\text{CH}_3\text{NH}_3\text{PbI}_3$ Perovskite Films: Evidence for Passivation Effect of PbI_2 . *J. Am. Chem. Soc.* **136**, 12205-12208 (2014).
11. Odenthal, P. et al. Spin-polarized exciton quantum beating in hybrid organic–inorganic perovskites. *Nat. Phys.* **13**, 894 (2017).
12. Ye, H.-Y. et al. Metal-free three-dimensional perovskite ferroelectrics. *Science* **361**, 151-155 (2018).
13. Frost, J.M. et al. Atomistic Origins of High-Performance in Hybrid Halide Perovskite Solar Cells. *Nano Lett.* **14**, 2584-2590 (2014).

14. Taylor, V.C.A. et al. Investigating the Role of the Organic Cation in Formamidinium Lead Iodide Perovskite Using Ultrafast Spectroscopy. *J. Phys. Chem. Lett.* **9**, 895-901 (2018).
15. Motta, C. et al. Revealing the role of organic cations in hybrid halide perovskite $\text{CH}_3\text{NH}_3\text{PbI}_3$. *Nat. Commun.* **6**, 7026 (2015).
16. Zheng, F., Tan, L.Z., Liu, S. & Rappe, A.M. Rashba Spin–Orbit Coupling Enhanced Carrier Lifetime in $\text{CH}_3\text{NH}_3\text{PbI}_3$. *Nano Lett.* **15**, 7794-7800 (2015).
17. Frohna, K. et al. Inversion symmetry and bulk Rashba effect in methylammonium lead iodide perovskite single crystals. *Nat. Commun.* **9**, 1829 (2018).
18. Yang, W.S. et al. High-performance photovoltaic perovskite layers fabricated through intramolecular exchange. *Science* **348**, 1234-1237 (2015).
19. Haiming, Z. et al. Organic Cations Might Not Be Essential to the Remarkable Properties of Band Edge Carriers in Lead Halide Perovskites. *Adv. Mater.* **29**, 1603072 (2017).
20. Kulbak, M., Cahen, D. & Hodes, G. How Important Is the Organic Part of Lead Halide Perovskite Photovoltaic Cells? Efficient CsPbBr_3 Cells. *J. Phys. Chem. Lett.* **6**, 2452-2456 (2015).
21. Zhu, H. et al. Screening in crystalline liquids protects energetic carriers in hybrid perovskites. *Science* **353**, 1409-1413 (2016).
22. Wu, X. et al. Trap States in Lead Iodide Perovskites. *J. Am. Chem. Soc.* **137**, 2089-2096 (2015).
23. Stoumpos, C.C. & Kanatzidis, M.G. The Renaissance of Halide Perovskites and Their Evolution as Emerging Semiconductors. *Acc. Chem. Res.* **48**, 2791-2802 (2015).
24. Guo, P. et al. Slow thermal equilibration in methylammonium lead iodide revealed by transient mid-infrared spectroscopy. *Nat. Commun.* **9**, 2792 (2018).
25. Whitfield, P.S. et al. Structures, Phase Transitions and Tricritical Behavior of the Hybrid Perovskite Methyl Ammonium Lead Iodide. *Sci. Rep.* **6**, 35685 (2016).
26. Yang, Y. et al. Large polarization-dependent exciton optical Stark effect in lead iodide perovskites. *Nat. Commun.* **7**, 12613 (2016).
27. Elles, C.G., Cox, M.J. & Crim, F.F. Vibrational relaxation of CH_3I in the gas phase and in solution. *J. Chem. Phys.* **120**, 6973-6979 (2004).

28. Davies, C.L. et al. Bimolecular recombination in methylammonium lead triiodide perovskite is an inverse absorption process. *Nat. Commun.* **9**, 293 (2018).
29. Stoumpos, C.C. et al. Ruddlesden–Popper Hybrid Lead Iodide Perovskite 2D Homologous Semiconductors. *Chem. Mater.* **28**, 2852-2867 (2016).
30. Wright, A.D. et al. Electron–phonon coupling in hybrid lead halide perovskites. *Nat. Commun.* **7**, 11755 (2016).
31. L., M.R., E., E.G., J., S.H., B., J.M. & M., H.L. Temperature-Dependent Charge-Carrier Dynamics in CH₃NH₃PbI₃ Perovskite Thin Films. *Adv. Funct. Mater.* **25**, 6218-6227 (2015).
32. Onoda-Yamamuro, N., Matsuo, T. & Suga, H. Calorimetric and IR spectroscopic studies of phase transitions in methylammonium trihalogenoplumbates (II)[†]. *J. Phys. Chem. Solids* **51**, 1383-1395 (1990).
33. Hutter, E.M. et al. Vapour-Deposited Cesium Lead Iodide Perovskites: Microsecond Charge Carrier Lifetimes and Enhanced Photovoltaic Performance. *ACS Energy Lett.* **2**, 1901-1908 (2017).
34. Wang, P. et al. Solvent-controlled growth of inorganic perovskite films in dry environment for efficient and stable solar cells. *Nat. Commun.* **9**, 2225 (2018).
35. Price, M.B. et al. Hot-carrier cooling and photoinduced refractive index changes in organic–inorganic lead halide perovskites. *Nat. Commun.* **6**, 8420 (2015).
36. Guo, Z. et al. Long-range hot-carrier transport in hybrid perovskites visualized by ultrafast microscopy. *Science* **356**, 59-62 (2017).
37. Ong, W.-L. et al. Orientational order controls crystalline and amorphous thermal transport in superatomic crystals. *Nat. Mater.* **16**, 83 (2016).
38. Mengjin, Y. et al. Square-Centimeter Solution-Processed Planar CH₃NH₃PbI₃ Perovskite Solar Cells with Efficiency Exceeding 15%. *Adv. Mater.* **27**, 6363-6370 (2015).

The submitted manuscript has been created by UChicago Argonne, LLC, Operator of Argonne National Laboratory ("Argonne"). Argonne, a U.S. Department of Energy Office of Science laboratory, is operated under Contract No. DE-AC02-06CH11357. The U.S. Government retains for itself, and others acting on its behalf, a paid-up nonexclusive, irrevocable worldwide license in said article to reproduce, prepare derivative works, distribute copies to the public, and perform publicly and display publicly, by or on behalf of the Government. The Department of Energy will provide public access to these results of federally sponsored research in accordance with the DOE Public Access Plan.
<http://energy.gov/downloads/doe-public-access-plan>